INTERNATIONAL JOURNAL FOR NUMERICAL METHODS IN FLUIDS
Int. J. Numer. Meth. Fluids 2001; **35**: 617–642

Three-dimensional coarse large-eddy simulations of the flow above two-dimensional sinusoidal waves

M. V. Salvetti[a,*,1], R. Damiani[b] and F. Beux[c]

[a] *Dipartimento di Ingegneria Aerospaziale, Università di Pisa, Via G. Caruso 2, 56126, Pisa, Italy*
[b] *Centro TEA, Consorzio Pisa Ricerche, Piazza D'Ancona 1, 56127, Pisa, Italy*
[c] *Scuola Normale Superiore, Piazza dei Cavalieri 7, 56126, Pisa, Italy*

SUMMARY

Large-eddy simulations (LES) of the flow over two-dimensional sinusoidal waves with a very low grid resolution are presented. A dynamic two-parameter subgrid scale (SGS) model is employed. A configuration characterized by a wave length of 0.6096 m, a maximum slope of 0.497, and a bulk velocity of 10 m s^{-1} is initially considered. Comparisons with experimental data, and with the results of a previous LES show that, in spite of the very low grid resolution, the mean flow and both the viscous and the pressure drag forces are well predicted. Some details of the flow, such as the presence of a secondary flow, are also captured. Thus, additional LES are carried out to investigate the effect of the Reynolds number (Re), and of the wave amplitude. In particular, the dependence of viscous and pressure drag on these parameters is studied and compared with the results of similar analyses in the literature. Copyright © 2001 John Wiley & Sons, Ltd.

KEY WORDS: coarse large-eddy simulation; friction drag; pressure drag; sinusoidal waves

1. INTRODUCTION

Turbulent flow over wavy terrains is of great interest to many environmental and engineering applications, and there have been many studies on this subject (see Reference [1] for a review). In particular, it has been shown that wavy terrains exert a net drag on turbulent flow over them, and this is primarily communicated by the pressure field. It has been observed that the incorporation of orographic drag from boundary-layer flow over hills can lead to an important improvement of numerical weather predictions. However, the scales of orography contributing to such a drag are usually smaller than those resolved in weather-prediction/climate models, and thus, the orographic drag must be introduced as an external parameter. An accurate parameterization of wind–wave exchanges is also needed in the models of air–sea wave interaction processes [2].

* Correspondence to: Dipartimento di Ingegneria Aerospaziale, Via G. Caruso 2, 56126 Pisa, Italy. Tel.: + 39 50 550200; fax: + 39 50 553654.
[1] E-mail: mv.salvetti@ing.unipi.it

Received November 1999
Revised May 2000

As in many other problems, numerical simulation can be a useful complementary tool, together with experimental and analytical studies. Direct numerical simulations of channel flow over wavy surfaces (see, for instance, References [3,4]) have not only successfully reproduced many of the laboratory observations, but have also provided a large number of details on the flow structure. However, direct numerical simulation is limited to low Reynolds numbers (*Re*), and hence, to small wave dimensions. Thus, to simulate the flows of interest in most of the applications, a turbulence model is needed. However, it is known [1] that simulations based on the *Re*-averaged Navier–Stokes equations (RANS), with classical eddy-viscosity closure models, are not appropriate to describe a large part of the flow; in particular, the so-called 'outer region', in which turbulent eddies are advected over the wave more rapidly than they interact each other. Other difficulties are related to the recirculating zones that occur in the leeward side of likewise moderate steep waves. The use of more complex full second-order closure models, as for instance in Reference [5], is a possibility; however, the flow structure itself suggests that LES could be a useful tool in tackling this type of flow, as also pointed out in Reference [1]. Indeed, a few examples can be found in the literature of LES of the convective boundary-layer [6–8], and, more recently, of the channel flow over sinusoidal wavy surfaces [9–11]. However, it also arises that, for LES, the grid resolution is a critical problem. Indeed, in Reference [10], the authors state that the lowest grid level should be in the viscous sub-layer, i.e., within approximately ten wall units, and in their LES, they use an even finer vertical grid spacing near the wall. A similar near wall resolution is used in Reference [11]. As a consequence, the *Re* of the flows simulated in References [10,11] are moderate. A less resolved LES of higher *Re* flows is documented in Reference [9]. Nonetheless, although the LES prediction of the shear stress agrees well with experimental data, the pressure drag is largely underestimated. Finally, the problem of grid resolution in LES of the flow over wavy surface is also pointed out in Reference [1], while, among the features suggested in Wood N., submitted, 1998, for a well designed LES of flows over complex terrains, one finds the requirement for the first grid point to be within the inner surface layer, which is usually of the order of one tenth of the inner region, i.e., a very thin layer indeed in real flows (see Reference [1]).

Clearly, if LES is to be used as a predictive tool for practical applications, such as flows over ocean waves or hills, only a much coarser resolution can be achieved owing to computer limitations. The main goal of this paper is to investigate whether LES with very coarse resolution can at least successfully predict the pressure and viscous contributions to the surface drag over wavy terrains, and the wave effects on the mean flow. Thus, this study could give important indications of the capabilities of LES in predicting problems of practical interest in this field and, also, on the possibilities of using LES to derive parameterizations to be incorporated in more simplified models. To this purpose, we simulate the aerodynamically-smooth case considered in Reference [9], but with a computational grid having half of the nodes in each direction than that used in the simulations in Reference [9]. Thus, the neutrally stratified flow in a channel between a free-slip upper surface and fixed two-dimensional sinusoidal waves is considered, with a wave length of 0.6096 m, a maximum slope of 0.497 and a bulk velocity of 10 m s^{-1}. Clearly, the assumption of a two-dimensional sinusoidal wave geometry and of flow periodicity in the streamwise and spanwise directions represents significant simplifications compared with realistic flows over ocean waves or hills. However, to

our knowledge, well documented experimental and numerical data are available in the literature for only these simplified cases. Moreover, these types of flows contain most of the fluid dynamics complexity of practical flows, such as, for instance, flow distortion or separated wakes, and thus, they are well suited for validation.

Generally, in LES and, in particular, when a very coarse grid resolution is used, a critical point is the modeling of the subgrid scale (SGS) terms. In References [9,10], the SGS terms are modeled by an eddy-viscosity, which is a function of the SGS kinetic energy, obtained by solving an additional transport equation. In our opinion, eddy-viscosity SGS models are not suited for the flows under investigation, for the same reasons as the RANS closure models based on eddy-viscosity concepts. Conversely, dynamic mixed models, [12–14], which include an eddy-viscosity part, as well as a scale-similar contribution, have recently shown a good behavior also for non-equilibrium flows [11,15]. Moreover, these models do not require the solution of any additional differential equation, and do not contain any *ad hoc* adjusted coefficient, as the model parameters are computed dynamically [16] from the resolved flow field. Thus, the two-parameter dynamic model proposed in Reference [14] is used in the present study.

The results obtained in the present LES are appraised by comparison with the experimental and LES data reported in Reference [9]. As good agreement is observed, additional LES simulations are carried out to study the effect of bulk velocity and wave amplitude. In particular, concerning the wave amplitude, comparisons are provided with the results of the simulations at lower *Re*, described in Reference [10].

2. PROBLEM FORMULATION

2.1. SGS modeling and numerical method

For the incompressible and neutrally stratified flows considered here, the governing equations are the Navier–Stokes and continuity equations (omitted here for sake of brevity). When a filter is applied to these equations, the effects of the unresolved SGS appear in the SGS stress tensor as:

$$\tau_{ij} = \overline{u_i u_j} - \bar{u}_i \bar{u}_j \tag{1}$$

in which u_i is the velocity component in the i direction, and the overbar denotes the filtering operation.

The SGS effect is modelled by the dynamic two-parameter model, proposed by Salvetti and Banerjee [14], in which the SGS stress tensor has the following expression:

$$\tau_{ij} - \frac{\delta_{ij}}{3}\tau_{kk} = -2C\bar{\Delta}^2|\bar{S}|\bar{S}_{ij} + K\left(L^m_{ij} - \frac{\delta_{ij}}{3}L^m_{kk}\right) \tag{2}$$

where $\bar{\Delta}$ is the filter width, and $\bar{S}_{ij}$ is the resolved strain rate tensor:

$$\bar{S}_{ij} = \frac{1}{2}\left(\frac{\partial \bar{u}_i}{\partial x_j} + \frac{\partial \bar{u}_j}{\partial x_i}\right)$$

and $|\bar{S}| = (2\bar{S}_{ij}\bar{S}_{ij})^{1/2}$; $L_{ij}^m = \overline{\bar{u}_i\bar{u}_j} - \bar{\bar{u}}_i\bar{\bar{u}}_j$ is the modified Leonard term, and represents the resolved part of the SGS stress. The two unknown coefficients C and K can be computed locally, following the dynamic procedure [16], as shown in Reference [14]. This model is stable only with local averaging of the model coefficients [17].

For our computations, the governing equations are transformed into a general curvilinear coordinate system, and discretized on a co-located grid using a finite volume approach, following the technique proposed in Reference [18]. The solver uses two sets of variables, defining Cartesian velocities and pressures at cell centers, and contravariant volume fluxes at the cell faces. A fractional step method is employed, and the pressure is obtained by solving a Poisson equation with a multigrid algorithm. Time marching is semi-implicit; the global formal accuracy is second order in both space and time. The details of the numerical method can be found in References [18,19]. This numerical approach has been extensively validated [18], and has been successfully used with dynamic mixed SGS models in previous LES of different types of flows [12,17,20,21]. Recently, the same numerical solver and the two-parameter dynamic SGS model have also been employed in a highly resolved LES over sinusoidal waves at lower Re [11].

2.2. Flow conditions

The flow over fixed two-dimensional sinusoidal waves has been considered, with the same geometry and conditions as found in Reference [9].

The domain size is given as $2\lambda \times 2\lambda \times \lambda$, respectively, along the x, y and z direction (Figure 1); λ denotes the wave length and, as in Reference [9], is equal to 0.6096 m.

The wave shape is taken as follows:

$$z(x) = a\cos(kx) \tag{3}$$

where $k = 2\pi/\lambda$ is the wave number and a is the wave amplitude. The first simulations assume $a = 0.04825$ m, resulting in $2a/\lambda \simeq 0.158$ and maximum slope $ak \simeq 0.497$.

Periodicity is imposed both along streamwise (x) and spanwise (y) directions. The wavy lower boundary in the vertical direction is considered no-slip, while the top boundary is considered free-slip and stress-free. The flow situation is illustrated in Figure 1(a).

The flow is driven by a mean pressure gradient; as no details of its value are provided in Reference [9], it has been computed according to the procedure discussed below.

For an open channel, i.e., a channel with a no-slip flat wall and a free-slip and stress-free upper boundary, the following relationship can easily be demonstrated:

$$u_* = \sqrt{\frac{\nabla_x p\, H}{\rho}} \tag{4}$$

in which H is the height of the channel, ρ is the fluid density, $\nabla_x p$ is the streamwise pressure gradient which drives the flow, and u_* is the effective friction velocity.

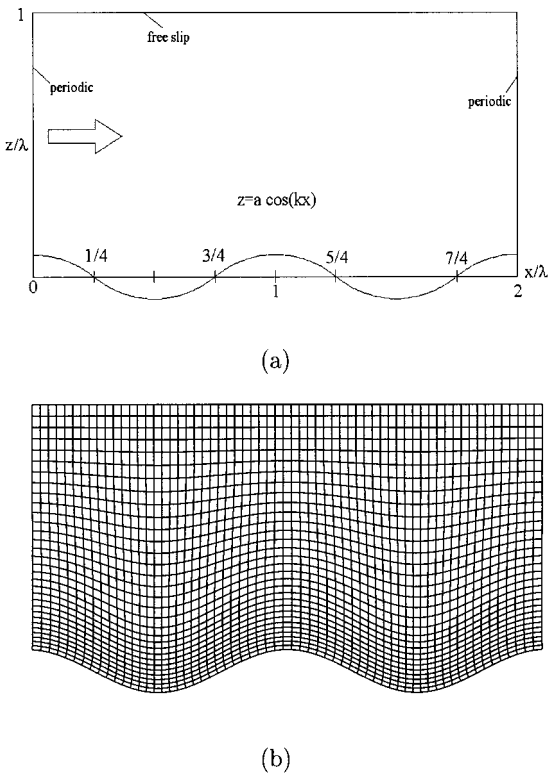

Figure 1. Sketch of a vertical section of the computational domain (a) and grid (b).

When the lower wall has a wavy shape, Equation (4) is no longer valid, and it is not that simple to achieve a relationship between the pressure gradient and the friction velocity. We thus follow De Angelis *et al.* [3], who give a correction factor to correlate the mean pressure gradient to the effective friction velocity:

$$u_* = C_1 \sqrt{\frac{\nabla_x p \, H}{\rho}} \tag{5}$$

The constant C_1 is obtained by extrapolating the results in Reference [3] given for certain a/λ ratios. Taking a/λ equal to 0.079, as in the present case, a value of 0.6824 is determined for C_1. Then, reverting Equation (5), we obtain the required gradient once the friction velocity has been fixed. In the first part of this study, we assume, as in Reference [9]: $u_* = 0.45 \text{ m s}^{-1}$, and a surface roughness $z_0 = 0.00003$ m, which corresponds to the relatively smooth case in Reference [9].

In the experiments in Reference [9], the reference velocity is taken equal to the freestream velocity, $U_0 = 10$ m s^{-1}. Clearly, because of the periodic boundary conditions employed in the simulations, the concept of freestream velocity does not apply; however, for sake of consistency, we decided to use the same value as in Reference [9] to adimensionalize the LES results. Let us consider the bulk velocity, defined as the average velocity computed along the height $H(x)$ of the channel:

$$\tilde{U}_b(x) = \frac{1}{H(x)} \int_0^{H(x)} U(x, z)\, \mathrm{d}z \tag{6}$$

in which $U(x, z)$ is the streamwise velocity averaged in time and in the y direction. As the mass flux is constant and the depth of the channel varies along x, the bulk velocity also varies along the streamwise coordinate. It will be verified in the next section that the average in the streamwise direction of $\tilde{U}_b(x)$ is close to U_0, and thus, in our case, the reference velocity represents a mean bulk velocity, U_b.

In Table I, we summarize the values of the *Re*, based on different quantities, in this first simulation.

The computational grid has $64 \times 64 \times 32$ nodes along x, y and z, respectively. It is uniform in the streamwise and spanwise directions, while in the vertical direction, nodes are clustered near the wavy wall (see Figure 1(b)). Note that our grid has half of the points in each direction than that used in Reference [9]; indeed, as discussed in the 'Introduction' section, one of the aims of the present work is to investigate whether an LES with a very coarse grid resolution can reproduce at least the global effects of waves on the flow. However, we decided to use a stretched grid in the z direction to have at least one computational point in the so-called 'inner region' near the surface (see Reference [1]). The height of this region, l, can be estimated, as suggested in Reference [1], from the following equation:

$$l \sim 0.5\kappa^2 \lambda \log^{-1}\left(\frac{l}{z_0}\right) \tag{7}$$

In our case, this gives $l \sim 0.0086$ m and $l^+ = lu_*/\nu \sim 275$. The first computational point is at a distance of approximately 146.7 wall units from the wavy surface, and the minimum grid spacing is $\Delta z^+ \simeq 293$, while near the upper boundary, it becomes $\Delta z^+ \simeq 775$. Consequently, our vertical grid resolution immediately close to the wall is approximately the same as in Reference [9], in which a uniform grid in all directions has been used. However, note that it is much larger than in the LES carried out for lower *Re* in References [10,11].

Table I. Parameters related to the simulation

$U_0 \simeq U_b$	$\nabla_x p$	u_*	Re_H	Re_{z_0}	Re_a	T_{ref}
10 m s^{-1}	0.88 N m^{-3}	0.45 m s^{-1}	417 500	0.92	33000	0.0609 s

$Re_H = U_b \cdot H/\nu$, $Re_{z_0} = u_* \cdot z_0/\nu$, $Re_a = U_b \cdot a/\nu$, $T_{\mathrm{ref}} = \lambda/U_0$.

Finally, if we had followed the recommendations given in Wood N., submitted, 1998, for a 'well designed' LES of the flow over wavy walls, the global number of points would have been:

$$3 \times 2 \times 270 \times \left(\frac{n}{2}\right)^3 \left(\frac{Z_i}{\lambda}\right)^3 \left(\frac{\lambda}{z_0}\right)^{1.65} \tag{8}$$

in which n is the number of computational points in the inner surface layer and Z_i is the boundary layer depth. In our case, by taking $n = 2$ and $Z_i \simeq \lambda$, Equation (8) would give approximately 2400 computational points in each direction.

The time step is equal to 1.5×10^{-4} s, and has been chosen in order to ensure the stability of the numerical method, which is explicit in the treatment of the convective terms. Clearly, this time step corresponds to a time resolution much higher than that in space.

3. RESULTS AND DISCUSSION

3.1. Validation

Mean velocity values are computed by averaging the field over the spanwise direction. In Reference [9], this is carried out from a single instantaneous field around $t = 16\ T_{\text{ref}}$. The reference time is defined as $T_{\text{ref}} = \lambda / U_0$. In Figure 2 we show that, in our simulation, a perfect periodicity has not yet been achieved around 16 T_{ref}; this can be owing either to the different initial conditions or to the fact that we are using a smaller sampling ensemble, because our grid has half of the points in each direction of that employed in Reference [9]. Conversely, a

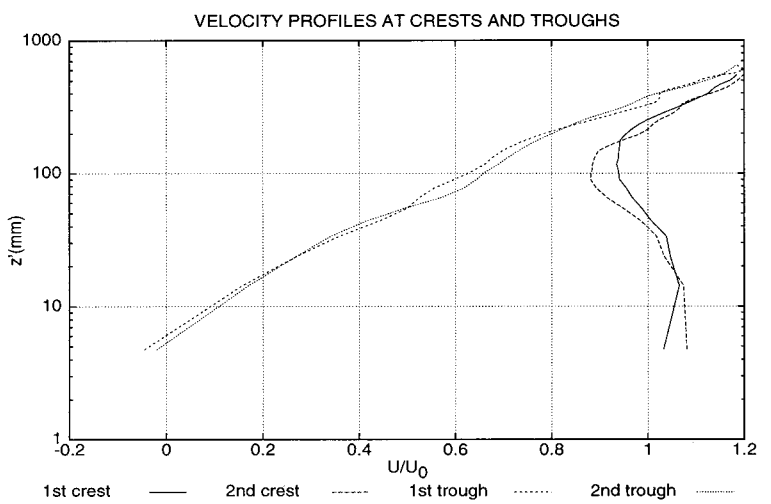

Figure 2. Mean u-velocity profiles above the crests and troughs. Data refer to $t = 16\ T_{\text{ref}}$. z' denotes the vertical distance from the wave surface.

practically periodic situation is obtained by averaging in time over quite a long interval ($\approx 7.4\ T_{\mathrm{ref}} = 0.45$ s), as can be seen in Figure 3. For this reason, we will refer to the latter mean values, and in the next pictures, data will be given, following Reference [9], averaging also among the same phase locations along the x direction. For the velocity distributions above the fourths of wavelength, we will keep profile data at $1/4\lambda$ and $5/4\lambda$ separated from one another owing to the larger bias.

In Figure 4, the profiles of the streamwise mean velocity, normalized by U_0, are presented above the crests and troughs of the waves, whereas in Figure 5, the profiles above the fourths of wavelength are shown. Our LES results are compared with the numerical and the experimental ones taken from Reference [9].

From these profiles, we computed the mean bulk velocity, U_b, as explained in Subsection 2.2. The calculated U_b is 9.6 m s^{-1}, which correlates well to the fixed U_0 and, thus, gives an *a posteriori* support to the mean pressure gradient calculation.

From Figures 4 and 5, we can assert that our results are in general good agreement with those given in Reference [9] but, especially for profiles above the crests, we may appreciate a better correspondence with the experiments.

However, in our simulations, reversed flow is appreciable near the wave troughs, even after quite a long averaging in time, while it is not present in the mean velocity profiles obtained in both experiments and calculations in Reference [9]. Nonetheless, it is pointed out in Reference [9] that flow separation was expected in troughs, as the maximum slope of the present case in 0.497 and $ak \simeq 0.3$ is generally considered to be the critical slope for separation, although there is some Re dependence. The experimental mean velocity profiles in Reference [9] were obtained from hot-wire probes, which can not differentiate between positive and negative velocities, and

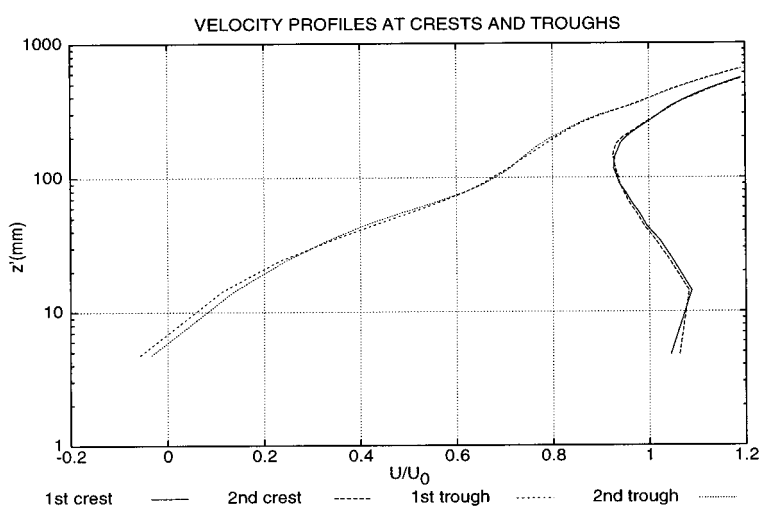

Figure 3. Mean u-velocity profiles above the crests and troughs. Data refer to average over time $\Delta t \approx 7.4\ T_{\mathrm{ref}}$.

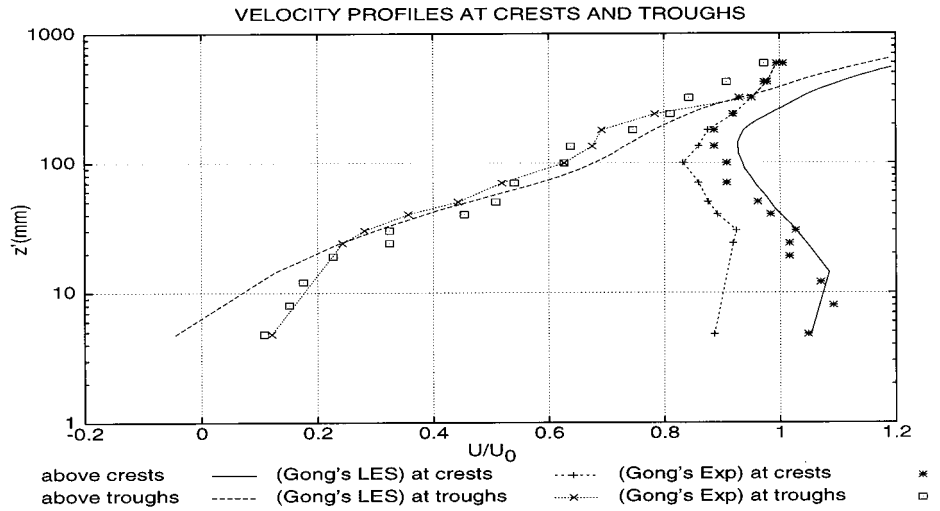

Figure 4. Mean u-velocity profiles above the crests and troughs.

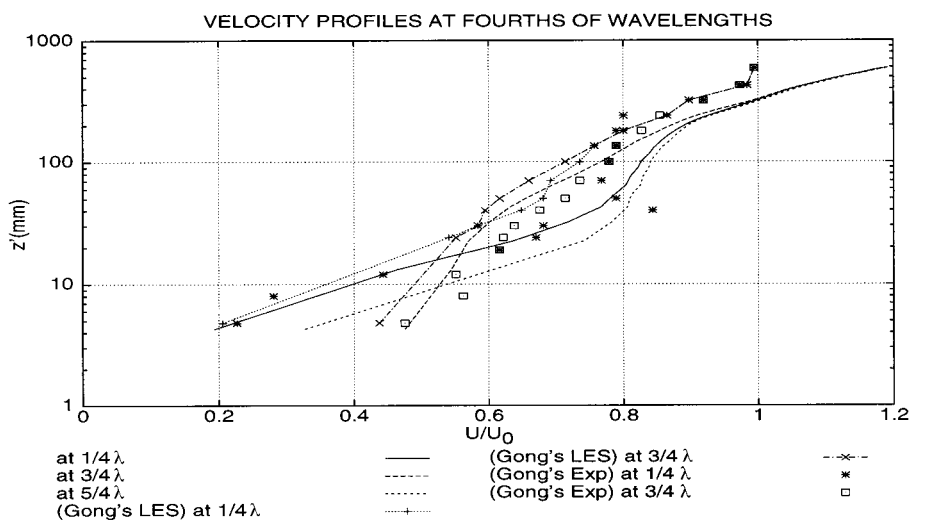

Figure 5. Time-average u-velocity profiles above fourths of wavelength.

are thus unreliable to detect recirculating flow. However, from tufts tests and pressure measurements, the authors conclude that their 'subjective interpretation is that there is little or no reverse flow'. The LES results in Reference [9] seem to give a support to this interpretation,

as recirculations are observed only temporarily, without any signature in the mean flow. Note, however, that the behavior of the flow in the downhill part of the wave observed in the LES in Reference [9] could be significantly affected by the underestimate of the mean flow acceleration in the uphill part of the wave. Thus, in our opinion, it is not clearly assessed by the data in Reference [9] that there is no reverse mean flow near the wave troughs.

Furthermore, near the upper boundary the velocity keeps increasing as far as $U/U_0 \simeq 1.2$, whereas data from Reference [9] do not seem to pass the value $U/U_0 \simeq 1$. The experiments agree with the latter result. This discrepancy could be owing to the fact that we are working with a mesh which has half of the points along the vertical direction than that used in Reference [9], and is stretched along z, so that the resolution near the top boundary of the channel is very poor. However, if the mean velocity profiles are computed later on in the simulation, e.g., after 30–40 T_{ref}, it has been found that U near the top boundary tends to U_0, in agreement with Reference [9]. As we are mainly interested in the behavior near the wavy wall, and this does not change significantly later on in the simulation, for our analysis, we just consider the profiles in Figures 4 and 5.

The spatial average of the streamwise component of the viscous stress, τ_{ns}, at the wall is evaluated as follows:

$$\langle \tau \rangle = \frac{1}{2\lambda} \int_0^{2\lambda} \tau_{\text{ns}} \sqrt{1 + \left(\frac{2\pi a}{\lambda}\right)^2 \left(\sin \frac{2\pi x}{\lambda}\right)^2} \, \mathrm{d}x \tag{9}$$

Obviously the integral in Equation (9) has to be discretized and τ_{ns} along the wave profile is determined from the friction velocity u_* computed at each x-location. A critical point in coarse simulations, as well as in experiments, is indeed the calculation of the friction velocity from the values of flow variables at the first available point near the wall. In order to make the comparison meaningful, we follow the same approach as in Reference [9], i.e., we assume the following logarithmic law satisfied for every z_2' along the ridge, z_2' being the distance from the wavy surface of the first computational point:

$$U(z') = \frac{u_*}{\kappa} \log\left(\frac{z' + z_0}{z_0}\right) \tag{10}$$

in which κ is the von Karman constant (we take $\kappa = 0.4$) and z' denotes the vertical distance from the wavy surface. As pointed out also in Reference [9], there is clearly some uncertainty about the accuracy of this approach, especially in separated regions. In Table II, we present both the mean viscous stress $\langle \tau_{\text{ns}} \rangle$ and its component along the streamwise direction, i.e., the viscous drag force per unit area $\langle \tau \rangle$, nondimensionalized with ρU_0^2. The result agrees well with the experimental value given by Reference [9] and, thus, our simulation seems to give good description of the shear stress near the waves, even with quite a coarse grid. This can also be seen from the distribution of the shear stress along the wave shown in Figure 6.

As far as the pressure drag is concerned, it is computed by averaging over 2λ the pressure only, whereas in Reference [9] they compute $\langle F_p \rangle$ as $\langle p + \overline{u_n'^2} \rangle$, where u_n' are the normal velocity fluctuations; thus, in our case, we obtain:

Table II. Mean viscous, pressure and total drag forces at the wavy wall

Variable	$\langle\tau_{ns}\rangle$	$\langle\tau\rangle$	$\langle F_p\rangle$	$\langle F_p\rangle+\langle\overline{u_n'^2}\rangle$	$\langle\tau\rangle+\langle F_p\rangle$
LES results	0.00219	0.0021	0.00844	0.00851	0.01061
LES [9]	–	0.0020	–	0.0027	0.0047
Exp [9]	–	0.0025	–	0.0085	0.0110

All forces are per unit area and normalized by ρU_0^2.

$$\rho U_0^2\langle F_p\rangle = -ak\frac{1}{2\lambda}\int_0^{2\lambda}\Delta p\,\sin(kx)\,\mathrm{d}x$$

Once more, you may notice a better agreement with the experimental values than that obtained in the LES in Reference [9].We also provide the average over 2λ of the quantity $p+\overline{u_n'^2}$; $\overline{u_n'^2}$ values are collected from the first grid points above the wavy surface. Though the result shows a perfect agreement with the one given in the experiments (see Table II) we will refer to $\langle F_p\rangle$ to indicate the form drag experienced by the wave.

An important finding in the experiments in Reference [9] was that an organized secondary flow developed, consisting in vortex pairs aligned with the mean flow. LES, although with some differences, qualitatively gave a support for the existence of this secondary flow. The presence of such a lateral flow has also been confirmed by more recent studies [3,10] and the mechanisms of its formation are presently a subject of investigation [11]. We briefly investigate here if such behavior also appears in our LES; however, we do not provide a detailed analysis of this phenomenon here, as it is in our opinion, beyond the scope of the present paper, and

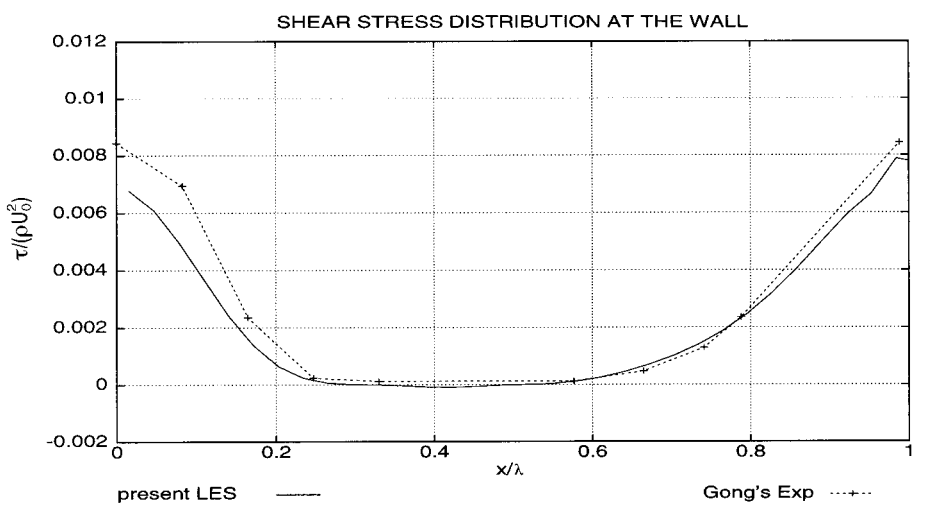

Figure 6. Distribution of the shear stress. Values are normalized dividing by ρU_0^2.

a coarse LES is probably not able to give all the details needed for a deeper physical investigation.

In Figure 7, the contour plots of $w' = w - \langle w \rangle$ are shown, at approximately 43 T_{ref}, at $z \simeq 0.15\lambda$; $\langle \cdot \rangle$ denotes here average in time, and in the y direction. As in Reference [9], only positive values are plotted to illustrate the vortical structures, which are characterized by alternating regions of positive and negative w'. From Figure 7, two regions of positive w' appear, which almost persist all over the length of the computational domain, indicative perhaps of two pairs of vortices with the axis almost aligned with the x direction. This conjecture is confirmed by the instantaneous (v, w) velocity vectors shown in Figure 8 for different streamwise stations at 43 T_{ref}. For instance, in the right part of the domain, two counter rotating vortices are clearly visible, also identified by streamlines. As can be seen, they persist along the wave and their centers are approximately at a constant height. Similar structures, although less well defined, can also be observed in the left part of the domain. The observations made from Figure 8 qualitatively agree well with the experimental findings in

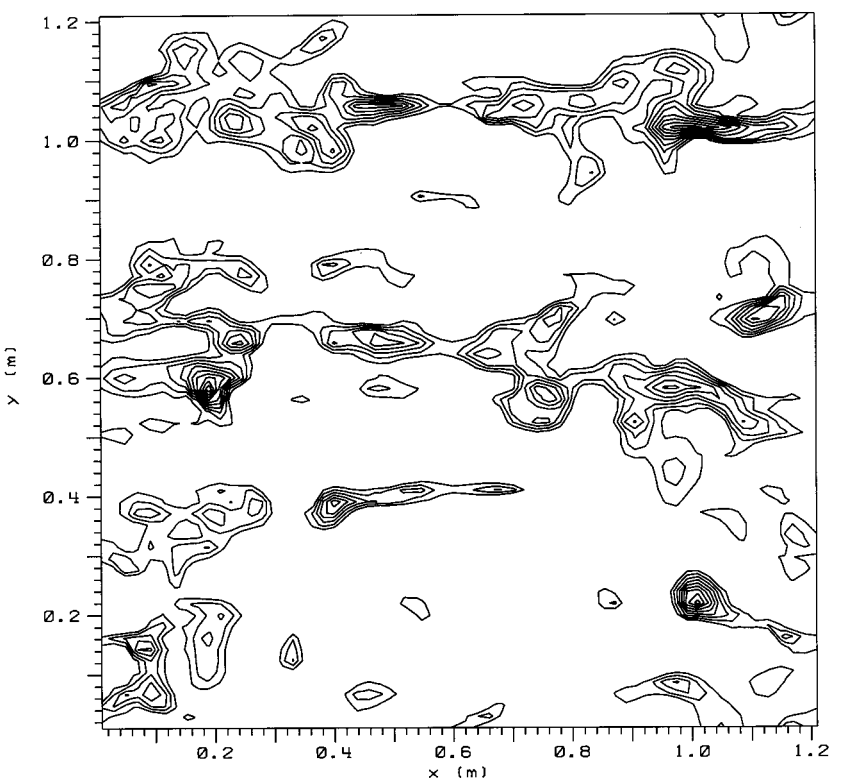

Figure 7. Contour plot of $w' = w - \langle w \rangle$ at approximately 43 T_{ref}. Positive contours only; the contour interval is $0.05U_0$.

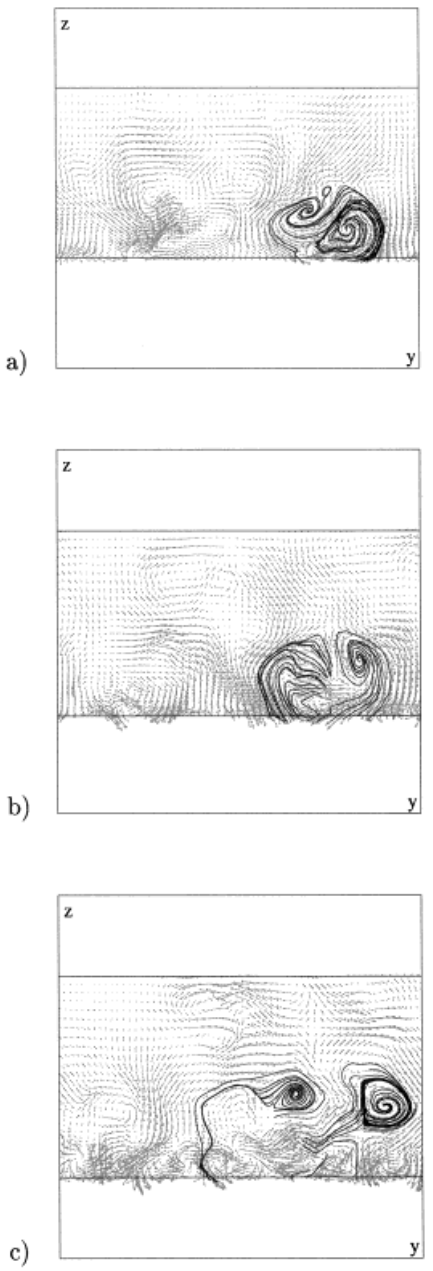

Figure 8. Instantaneous (v, w) velocity vectors at 43 T_{ref}. (a) Wave crest; (b) $\lambda/4$; (c) wave trough.

Reference [9]. In the LES in Reference [9] the presence of secondary flows was also observed, but no coherent vortices were clearly detectable.

In a coarse LES, such as that presented here, the SGS model is expected to give a significant contribution to the overall stress. The model employed here contains a part which is proportional to the Leonard term that is not present in the eddy-viscosity models used in previous LES of this type of flow [9,10]. Consistently with the results obtained in previous LES with mixed SGS models [12,17], the Leonard term has been found to provide almost the whole SGS stress. As an example, Figure 9 shows the contributions of the eddy-viscosity and Leonard terms to the 13 component of τ_{ij} (1 denotes the streamwise direction and 3 the normal one) above crests and troughs, averaged in time and over the spanwise direction, and adimensionalized by the mean shear stress at the wall $\tau = \rho u_*^2$. The same quantities are reported in Figure 10 at fourths of the wavelength. Note that at all locations, for the present coarse resolution, the Leonard term gives SGS stresses that are significantly larger than τ, and this SGS contribution is important whenever the shear in the flow is significant. This result is consistent with the findings of previous *a priori* tests [14] and LES of different flows [17]. As a consequence, at $\lambda = 1/4$ and above troughs, when the wave boundary layer is thicker or a recirculation zone is present, the SGS stresses tends also to be significant rather far from the wall. Similar considerations can also be made for the other components of τ_{ij} and for SGS energy dissipation (omitted here for sake of brevity). The parameter multiplying the Leonard term K, averaged in time and over all the computational domain, has been found to be equal to 1.2. This value is very similar to those found in *a priori* tests and LES for different flow

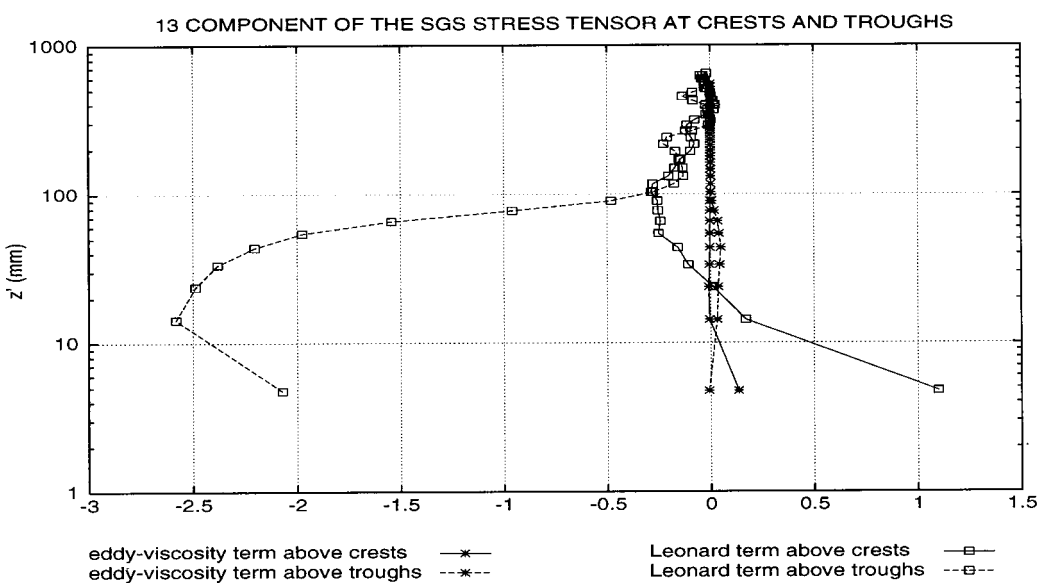

Figure 9. Mean τ_{13} component profiles above the crests and troughs.

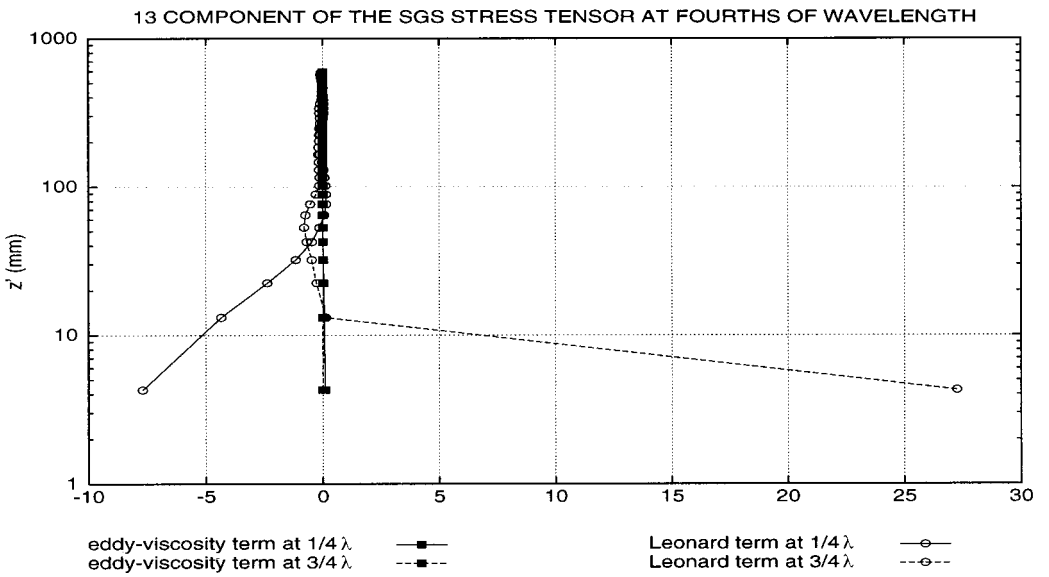

Figure 10. Mean τ_{13} component profiles above fourths of wavelength.

types at lower *Re* [14,17]; this indicates that the value of K obtained from the dynamic procedure is rather independent of the flow type and *Re*. Conversely, for this high *Re* flow and coarse grid resolution, the average ratio v_t/v has been found to be significanlty larger than in previous studies at lower *Re* [14,17] ($v_t/v \simeq 2.5$ in the present case). However, as discussed previously, also in this case, the eddy-viscosity term only gives a small contribution to SGS stresses and energy.

3.2. Effects of the bulk velocity

As it has previously been shown that our numerical approach is able to give an accurate prediction of the mean flow and forces at the wavy surface, LES is used here to study the effect of the *Re* on the flow over sinusoidal periodic waves.

The flow configuration is thus the same as in Subsection 3.1 and the *Re*s are varied by changing the mean bulk velocity and consequently the u_* value. New values for the mean pressure gradient are calculated according to the procedure described in Section 2, once the value of the bulk-velocity has been chosen. In Table III, the basic parameters of the different simulations are summarized. The simulation at $U_b = 10$ m s^{-1} is that described in detail in Subsection 3.1. For the lower U_b cases, the same grid has been used, while for $U_b = 12$ m s^{-1}, in order to maintain the same grid resolution as previously (i.e., the same Δx^+, Δy^+ and Δz^+), $80 \times 80 \times 40$ nodes have been used.

In Figure 11, the profiles of the mean velocity, normalized by U_0 (taken, as previously, equal to the mean bulk velocity) are presented above the crests and troughs of the waves, for the

Table III. Parameters related to simulations performed with different *Re*

U_b	$\nabla_x p$	u_*	Re_H	Re_{z_0}	Re_a	T_{ref}
12 m s^{-1}	1.2583 N m^{-3}	0.54 m s^{-1}	504 000	1.11	39 000	0.0508
10 m s^{-1}	0.88 N m^{-3}	0.45 m s^{-1}	417 500	0.92	33 000	0.0609
8 m s^{-1}	0.559 N m^{-3}	0.36 m s^{-1}	334 000	0.74	26 430	0.0762
6 m s^{-1}	0.314 N m^{-3}	0.27 m s^{-1}	250 500	0.55	19 800	0.1016

$Re_H = U_b \cdot H/\nu$, $Re_{z_0} = u_* \cdot z_0/\nu$, $Re_a = U_b \cdot a/\nu$, $T_{\text{ref}} = \lambda/U_0$.

different *Re*s. In Figure 12, the same profiles are shown above the fourths of wavelength. For the cases at $U_b = 8$ m s^{-1} and $U_b = 6$ m s^{-1}, the mean values have been obtained by averaging in time over $\Delta t \approx 7.4\ T_{\text{ref}}$ as in the other two cases, but starting after approximately 24 T_{ref}. Indeed, these lower *Re* cases take longer to reach a periodic stabilized regime. Incidentally, note that, as mentioned in Subsection 3.1, when the mean values are gathered quite late in the simulation, the velocity near the upper boundary correctly tends to U_0. At all the considered locations, except than at troughs, the mean velocity values near the wall tend to decrease as the *Re* increases. This effect is more significant in the windward side of the wave (at $3/4\lambda$ and above the crest), meaning that the flow acceleration induced by the wall is noticeably decreased as the bulk velocity increases. As a consequence, the shear stress over the wave increases when the bulk velocity is decreased, as shown in Figure 13. This implies that the viscous drag coefficient $\langle \tau \rangle$ also increases for decreasing U_b, as can be seen in Table IV.

Coming back to Figure 11, note that for the highest *Re*, the reverse flow near the wave troughs has disappeared. This effect has also been observed in previous experimental studies

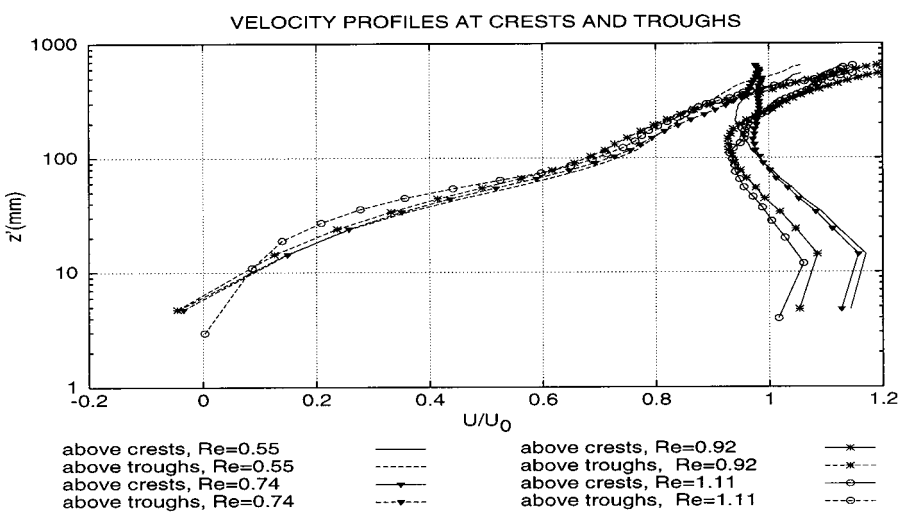

Figure 11. Mean u-velocity profiles above the crests and troughs for different *Re*.

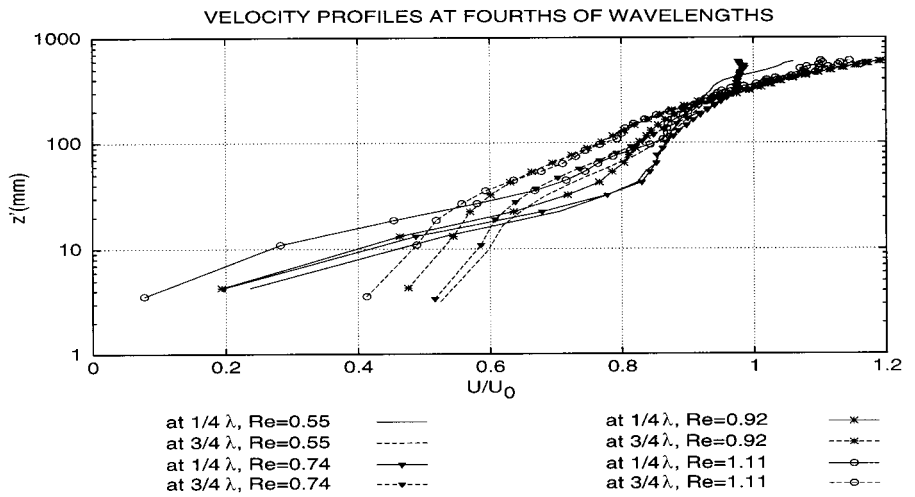

Figure 12. Time-average u-velocity profiles above fourths of wavelength for different Re.

(see, for instance, Reference [22]), and is consistent with the fact that the flow acceleration induced by the wave is lower as Re increases.

Another consequence is that, as the bulk velocity decreases, the pressure gradient along the wave becomes steeper, resulting in a larger suction at the wave crest (not shown here for sake

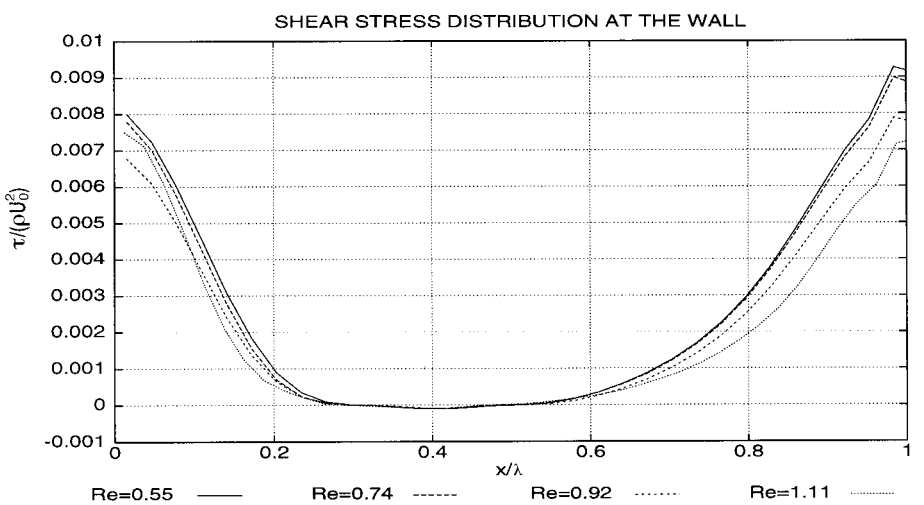

Figure 13. Distribution of the shear-stress for different Re. Values are normalized dividing by ρU_0^2.

Table IV. Mean viscous, pressure and total drag forces at the wavy wall for different Re

Re_{z_0}	$\langle\tau_{\mathrm{ns}}\rangle$	$\langle\tau\rangle$	$\langle F_p\rangle$	$\langle F_p\rangle+\langle\overline{u_n'^2}\rangle$	$\langle\tau\rangle+\langle F_p\rangle$
1.11	0.00203	0.00196	0.0078	0.00791	0.00976
0.92	0.00219	0.0021	0.0084	0.00851	0.01061
0.74	0.00252	0.0024	0.00964	0.00973	0.01204
0.55	0.00261	0.0025	0.00979	0.00988	0.01229

All forces are per unit area and normalized by ρU_0^2.

of brevity). Therefore, the pressure drag coefficient increases for decreasing U_b, as shown in Table IV.

In order to analyze in more detail the dependence on the Re, in Figure 14 the shear and pressure drag coefficients are reported as a function of $Re_\lambda = Re_H = U_b\lambda/\nu$. The value of $\langle\tau\rangle$ for a fully developed flat channel flow is also shown for comparison; we used the law proposed in Reference [23], $\langle\tau_{FP}\rangle = 0.0188 Re_\lambda^{-1/6}$, which is in good agreement with other results proposed in the literature. It can be seen that the behavior with Re of the friction drag coefficient obtained in our LES is similar to that of a flat channel flow; this was also found in the experiments in Reference [22] for lower Re.

More surprisingly also, the pressure drag coefficient $\langle F_p\rangle$ decreases with $Re_\lambda^{-1/6}$, like the viscous drag coefficient. Indeed, for all the Re, the pressure and viscous contributions represent the 80% and 20% of the total drag, respectively. A classical simple parameterization of the drag force per unit surface, based on analytical considerations for small amplitude sinusoidal waves, when $u_*/U_b \to 0$, is that proposed by Sykes [24]:

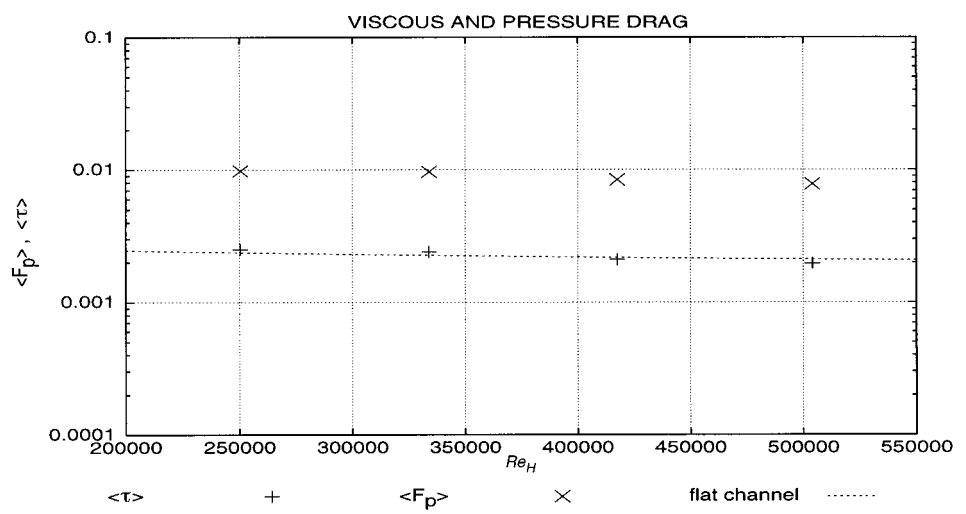

Figure 14. Viscous and form drag for different Re. Values are normalized dividing by ρU_0^2.

$$\rho U_0^2(\langle F_p \rangle + \langle \tau \rangle) \simeq \rho U_0^2 \langle F_p \rangle \propto (ak)^2 u_*^2 \tag{11}$$

in which u_* is the friction velocity of the upstream undisturbed flow. Although in our simulations, $u_*/U_b = 0.045$, the present results are in disagreement with formula (11). Indeed, the viscous drag always represents a not negligible contribution to the total drag; moreover the total drag force does not depend on u_*^2, but, consistent with the previous analysis and remembering that $U_b = U_0$, on $U_b^{11/6}$, and thus in our case, on $u_*^{11/6}$.

3.3. Effects of the wave shape

LES have been carried out also to investigate how the wave shape, particularly in terms of the a/λ ratio, could affect the flow characteristics. In Table V, the main flow parameters, computed following the procedures illustrated in the previous sections, are shown for these new simulations. As may be observed, the friction velocity and the bulk velocity are kept the same as in the LES described in Subsection 3.1 (for which $ak = 0.497$), together with the number of grid points ($64 \times 64 \times 32$). The wave shape has been varied by changing the amplitude. The wavelength, and hence, the domain dimensions, are kept constant.

In Figures 15 and 16 the mean u-velocity profiles are shown, adimensionalized as usual by $U_0 = U_b$. First of all, note that separation is visible in the mean flow only for $ak > 0.4$, and the reverse flow region never reaches the streamwise stations at $1/4\lambda$ and $3/4\lambda$. In our case also, at $ak = 0.35$, small recirculating flow regions are observed, although they are not apparent in the mean flow at the streamwise sections presented in Figures 15 and 16. Usually, $ak = 0.3$ is indicated as the critical value at which separation starts (see, for instance, the experiments in Reference [25] and the simulations in Reference [10]). This discrepancy, however, can be owing to the fact that the Re in our simulations is significantly higher than in References [10,25], and this has the effect of delaying the flow separation, as observed in the previous section and in Reference [22].

In our simulations, $ak = 0.35$ has been found to be a critical value also, as concerns the behavior of the mean velocity in the windward part of the wave. Indeed, up to $ak = 0.35$, the near wall velocity increases with the wave amplitude, while for $ak > 0.35$, the opposite trend is observed. This behavior is particularly evident near the wave crests, where the maximum of the near wall velocity is indeed obtained for $ak = 0.35$.

The distribution of the shear stress along the wave is reported in Figure 17. Note that, for $ak \geq 0.35$, the slope of the τ gradient is the same for all the wave amplitudes, while for

Table V. Main simulation parameters for the different wave shapes

ak	u_* (m s^{-1})	Re_{z_0}	Re_{Hd}	Re_a	λ (m)	a (m)	$\nabla_x p$ (N m^{-3})	C_1
0.25	0.45	0.92	417 500	16 700	0.6096	0.02425	0.5568	0.8549
0.35	0.45	0.92	417 500	23 350	0.6096	0.03396	0.6605	0.7849
0.4	0.45	0.92	417 500	26 700	0.6096	0.03881	0.7236	0.7499
0.497	0.45	0.92	417 500	33 000	0.6096	0.04825	0.88	0.6824
0.6	0.45	0.92	417 500	40 000	0.6096	0.05821	1.0942	0.6098

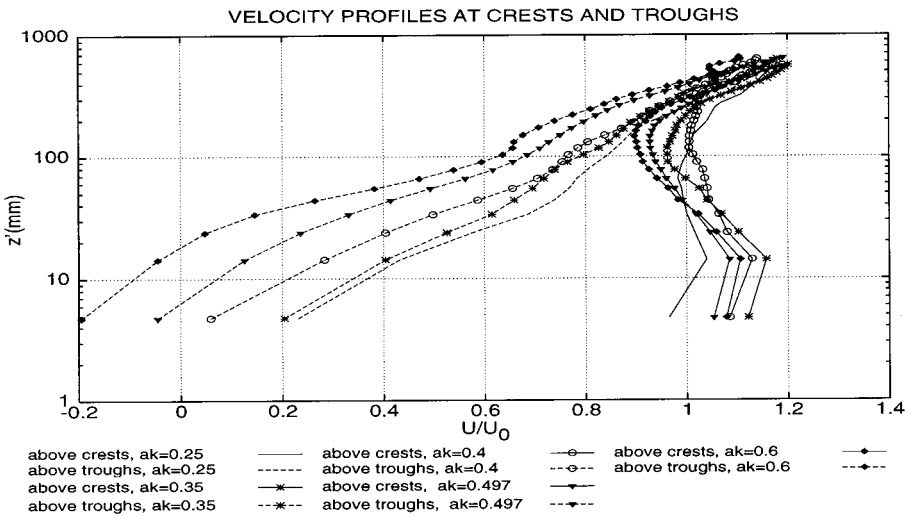

Figure 15. Mean u-velocity profiles above the crests and troughs for different different wave amplitudes.

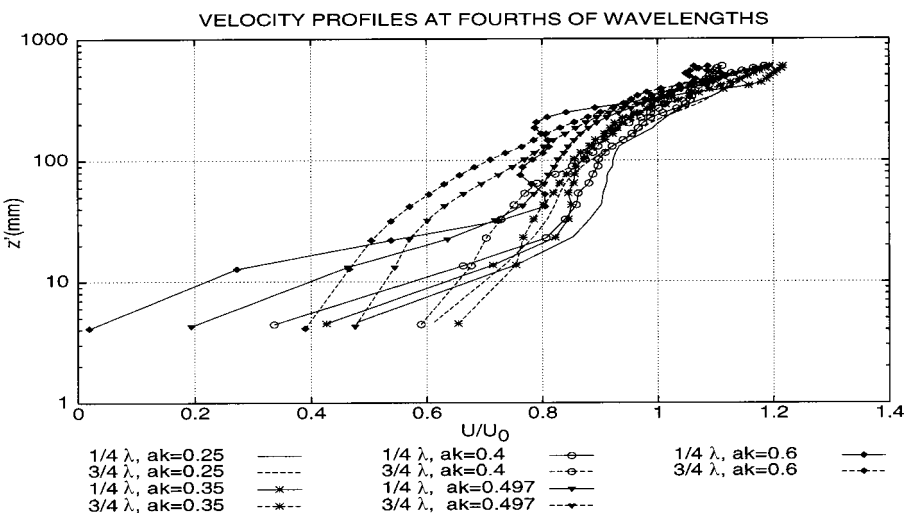

Figure 16. Mean u-velocity profiles above the fourths of wavelength for different different wave amplitudes.

$ak = 0.25$, it is significantly less steep and nearly symmetric, as found also for small slopes in Reference [10]. Consistent with the previous analysis of the mean velocity, the shear stress near the wall crests is maximum for $ak = 0.35$, especially in the windward side, and then decreases

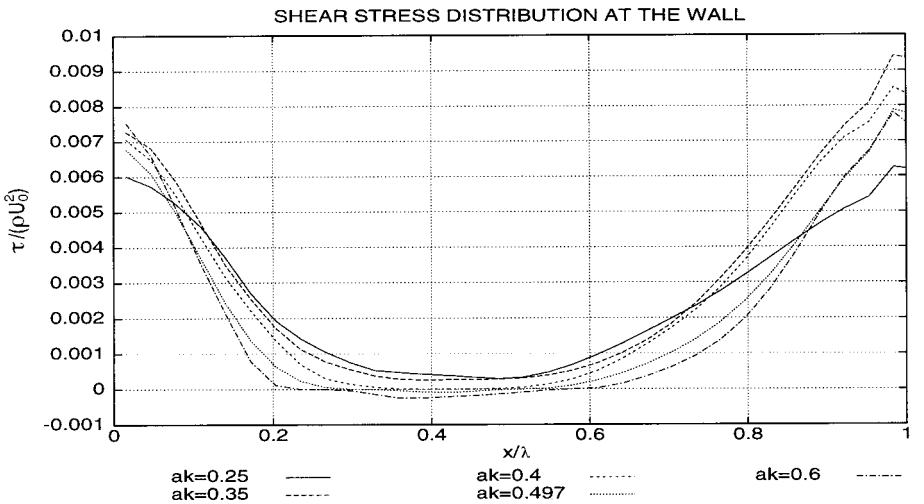

Figure 17. Wall shear stress ($\tau|w/(\rho U_0^2)$) distribution for the various analyzed wave amplitudes.

with the wave amplitude. As a consequence, the viscous drag per unit length averaged over the wave also shows a maximum for $ak = 0.35$ and decreases with increasing ak, as shown in Figure 18.

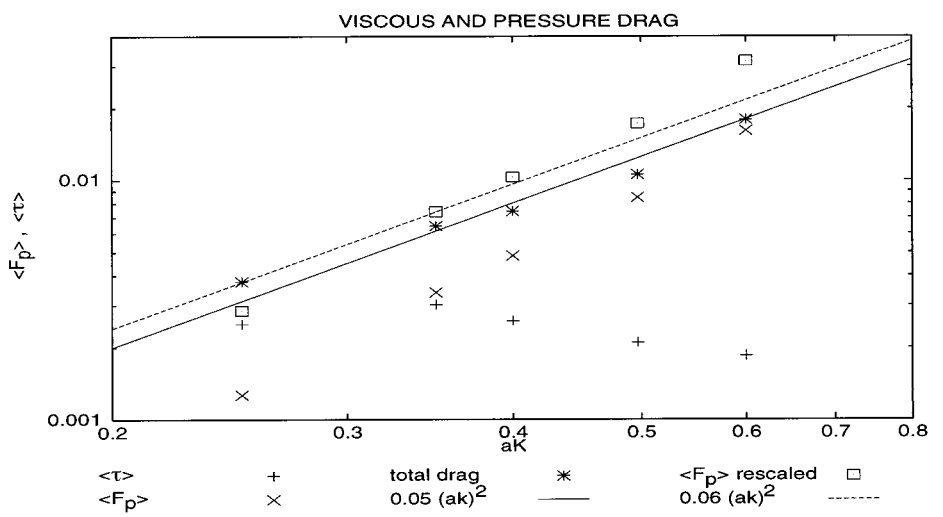

Figure 18. Viscous, pressure and total drag, normalized by ρU_0^2 for different wave amplitudes.

Following Equation (11), the pressure drag should be proportional to the square of ak; this has been confirmed by the LES in Reference [10], in which a good fit of the pressure drag coefficients, obtained for different wave amplitudes, has been found to be $0.12(ak)^2$. The coefficients $\langle F_p \rangle$ obtained in our simulations clearly show a steeper increase than $(ak)^2$. However, this is owing to the different normalization of our coefficients; indeed, to recover the definition of pressure drag coefficient used in Reference [10], we should multiply our values by approximately $2[(H-2a)/(H-a)]^2$. The rescaled coefficients, shown in Figure 18 by the open squares, can be fit by $0.06(ak)^2$. By assuming a dependence of the pressure drag coefficient on $Re_H^{-1/6}$, as found in Subsection 3.2, as the ratio between the Re in our simulations and those in the LES in Reference [10] is approximately 20, one can affirm that our results are also in a satisfactory quantitative agreement with those in Reference [10]. However, an increase in slope is observed for high values of ak, while a slight fall-off with slope is found in Reference [10], which seems to be consistent also with the analytical results in Reference [26]. This discrepancy could be owing to the higher Re in our simulations. Indeed, if the pressure distribution along the wave (not shown here for sake of brevity) is considered, for high values of ak, a significant peak is observed at the flow reattachment point, as found also in Reference [10]. However, in our case, this peak is significantly higher than in Reference [10], resulting in a larger pressure drag. A similar discrepancy was observed in Reference [10] by comparing the LES pressure distribution with the experimental one obtained in Reference [22] at a higher Re, and the authors suggest that 'there may be some Reynolds-number effect'.

A rather good fit of the total drag coefficient, normalized by ρU_0^2, is $0.05(ak)^2$. Finally, Figure 18 shows that, as expected, pressure drag tends to become the main part of the global drag, as the wave amplitude increases.

As concerns the lateral flow, it seems that, as the wave amplitude increases, the streamwise secondary vortices become more intense and persistent along the x direction. This can be seen from the normal velocity fluctuations iso-contours on a plane at a distance of 0.045λ from the wave crest, shown in Figures 19 and 20 for $ak = 0.25$ and $ak = 0.6$ respectively. Indeed, in the lowest amplitude case the regions of significant positive w' are clearly less and less persistent along the streamwise direction than for the highest amplitude case. These observations are confirmed also by the instantaneous velocity (v, w) vectors (not shown here for the sake of brevity). A similar trend, i.e., a transverse flow becoming more important with the wave steepness, was also observed in the LES in Reference [10], and it was used to explain the significant increase in lateral velocity variance close to the wave upslope surface. We do not provide here, however, an analysis of the lateral velocity variance, as it is, in our opinion, beyond the scope of the present paper.

4. CONCLUDING REMARKS

LES of the flow over two-dimensional sinusoidal waves have been presented. They have been carried out with a very low grid resolution, i.e., with minimum vertical grid spacing of about 300 wall units. A dynamic two-parameter SGS model has been employed. This model does not require the solution of additional transport equations nor *ad-hoc* tuned parameters.

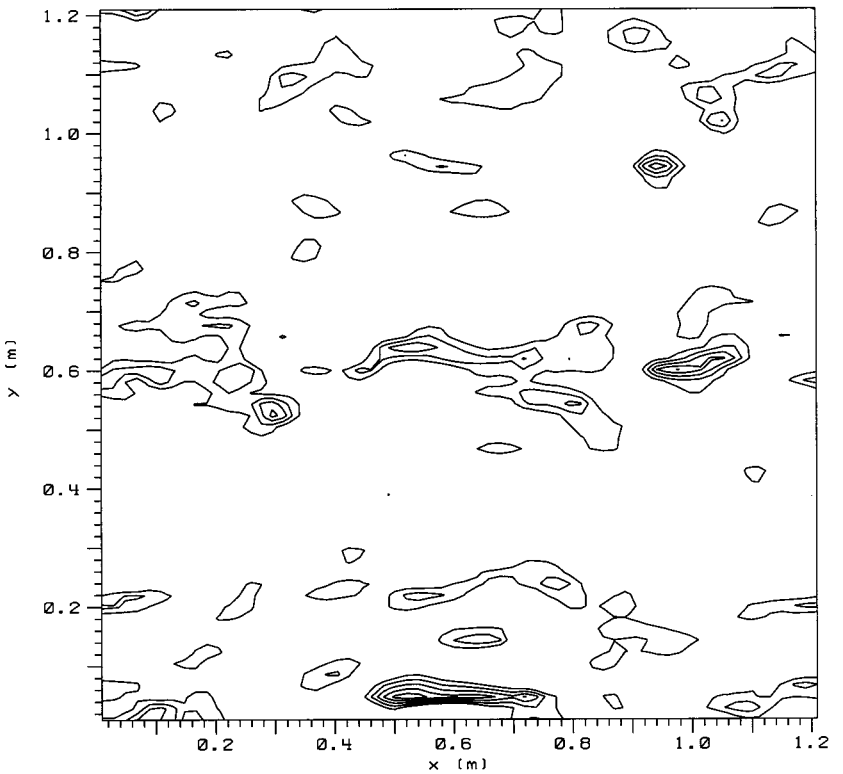

Figure 19. Contour plot of $w' = w - \langle w \rangle$ for $ak = 0.2$. Positive contours only; the contour interval is $0.05U_0$.

A configuration characterized by a wave length of 0.6096 m, a maximum slope of 0.497 and a bulk velocity of 10 m s^{-1} has been initially considered. The capability of such a coarse LES to capture, at least, the main features of the flow has been assessed by comparing our results with experimental data, and with those of a more resolved LES [9]. It has been shown that the mean flow and both viscous and pressure drag forces are well predicted. In spite of the lower grid resolution, the global agreement with the experimental data is better than that obtained in the previous LES in Reference [9]. This is probably owing to the different SGS models used in the simulations. Some details, such as the presence of a secondary flow, are also captured.

Then LES has been used to study the effects of the bulk velocity and of the wave amplitude. The increase of bulk velocity, and thus of *Re*, has been found to retard the flow separation, consistent with the experiment in Reference [22]. Both viscous and pressure drag coefficients have been found to decrease as $Re_{\lambda}^{-1/6}$ (or equivalently as $Re_{H}^{-1/6}$); the viscous and pressure relative contributions to the total drag remain constant when the bulk velocity varies. As concerns the wave amplitude effect, the pressure drag coefficients, opportunely rescaled, have

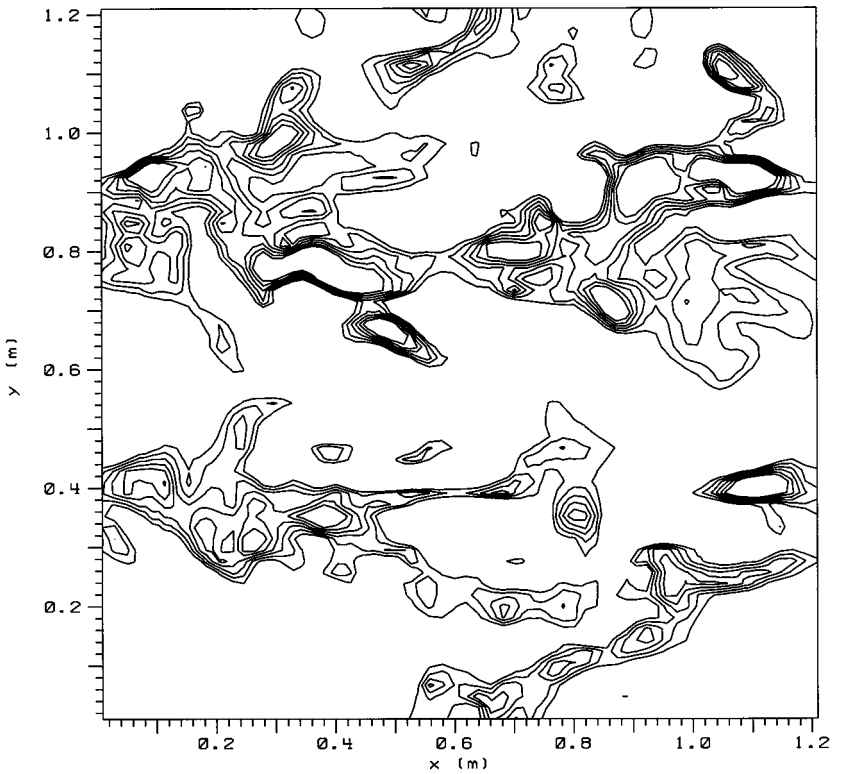

Figure 20. Contour plot of $w' = w - \langle w \rangle$ for $ak = 0.6$. Positive contours only; the contour interval is $0.05U_0$.

been found to increase with $(ak)^2$, as observed in Reference [10]. If the effects of the higher *Re* in our simulations is taken into account, a satisfactory quantitative agreement is also found with the results in Reference [10]. Conversely, the viscous drag shows a maximum at $ak = 0.35$, and then decreases. Indeed, the pressure drag tends to become the main part of the total drag with increasing *ak*. As concerns flow separation, zones of reverse flow are observed for $ak \geq 0.35$. This value is larger than those found in previous studies [10,22,25]. However, this could be owing to the higher *Re* of our simulations. Consistent with the experimental and numerical observations in References [10,22], the extent of the recirculating zones becomes larger with increasing *ak*. The intensity and the persistence of secondary streamwise vortices also increases with *ak*, and this is again in qualitative agreement with the findings in Reference [10].

From the present study one may conclude that coarse LES, with suitable SGS models, are able to predict the main features of the flow over wavy surfaces, and, in particular, the viscous and pressure surface drag and their dependence on the flow parameters. Thus, this LES

approach could be applied in the future to estimate the drag over waves of arbitrary shape, for instance representative of gravity ocean waves.

ACKNOWLEDGMENTS

M.V. Salvetti gratefully acknowledges Professor R.L. Street and Dr. Y. Zang for the permission to use and adapt their numerical code. This research has been supported by European Community under Contract ENV4-CT97-0460.

REFERENCES

1. Belcher SE, Hunt JCR. Turbulent flow over hills and waves. *Annual Review of Fluid Mechanics* 1998; **30**: 507.
2. Makin VK, Kudryavstev VN. Coupled sea surface-atmosphere model-1. Wind over wave coupling. *Journal of Geophysical Research—Oceans* 1999; **104**(4): 7613.
3. De Angelis V, Lombardi P, Banerjee S. Direct numerical simulation of turbulent flow over a wavy wall. *Physics of Fluids* 1997; **9**(8): 2429.
4. Cherukat P Na Y, Hanratty TJ, McLaughlin JB. Direct numerical simulation of a fully developed turbulent flow over a wavy wall. *Theoretical and Computational Fluid Dynamics* 1998; **11**: 109.
5. Mastenbroek C, Makin VK, Garat MH, Giovanangeli JP. Experimental evidence of the rapid distortion of turbulence in air flow over waves. *Journal of Fluid Mechanics* 1996; **318**: 273.
6. Krettenauer K, Schumann U. Numerical solution of turbulent convection over wavy terrain. *Journal of Fluid Mechanics* 1992; **237**: 261.
7. Walko RL, Cotton WR, Pielke RA. Large-eddy simulations of the effects of hilly terrain on the convective boundary layer. *Boundary-Layer Meteorology* 1992; **58**: 133.
8. Dörnbrack A, Schumann U. Numerical simulation of turbulent convective flow over wavy terrain. *Boundary-Layer Meteorology* 1993; **65**: 323.
9. Gong W, Taylor PA, Dörnbrack A. Turbulent boundary-layer flow over fixed aerodynamically rough two-dimensional sinusoidal waves. *Journal of Fluid Mechanics* 1996; **312**: 1.
10. Henn DS, Sykes RI. Large-eddy simulation of flow over wavy surfaces. *Journal of Fluid Mechanics* 1999; **383**: 75.
11. Calhoun RJ. Numerical investigations of turbulent flows over complex terrain (channel terrain, streamwise vortices), PhD Dissertation. Stanford University, 1998.
12. Zang Y, Street RL, Koseff JR. A dynamic mixed subgrid-scale model and its application to turbulent recirculating flows. *Physics of Fluids A* 1993; **5**: 3186.
13. Liu S, Menevau C, Katz J. On the properties of similarity subgrid-scale models as deduced from measurements in a turbulent jet. *Journal of Fluid Mechanics* 1994; **275**: 83.
14. Salvetti MV, Banerjee S. A priori tests of a new dynamic subgrid-scale model for finite-difference large-eddy simulations. *Physics of Fluids* 1995; **7**: 2831.
15. Sarghini F, Piomelli U, Balaras E. Scale-similar models for large-eddy simulations. *Physics of Fluids* 1999; **11**: 1596.
16. Germano M, Piomelli U, Moin P, Cabot WH. A dynamic subgrid-scale eddy-viscosity model. *Physics of Fluids A* 1991; **3**: 1760.
17. Salvetti MV, Zang Y, Street RL, Banerjee S. Large-eddy simulation of free-surface decaying turbulence with dynamic subgrid-scale models. *Physics of Fluids* 1997; **9**: 2405.
18. Zang Y, Street RL, Koseff JR. A non-staggered grid, fractional step method for time-dependent incompressible Navier–Stokes equations in general curvilinear coordinate systems. *Journal of Computational Physics* 1994; **114**: 18.
19. Zang Y, Street RL. A composite multigrid method for calculating unsteady incompressible flows in geometrically complex domains. *International Journal for Numerical Methods in Fluids* 1995; **20**: 341.
20. Zang Y, Street RL. Numerical simulation of coastal upwelling and interfacial instability of a rotating and stratified fluid. *Journal of Fluid Mechanics* 1995; **305**: 47.
21. Yuan LL, Street RL, Ferziger JH. Large-eddy simulations of a round jet in crossflow. *Journal of Fluid Mechanics* 1999; **379**: 71.
22. Zilker DP, Hanratty TJ. Influence of the amplitude of a solid wavy wall on a turbulent flow. Part 2. Separated flows. *Journal of Fluid Mechanics* 1979; **90**(2): 257.

23. Patel VC, Head MR. Some observations on skin friction and velocity profiles in fully developed pipe and channel flows. *Journal of Fluid Mechanics* 1969; **38**: 181.
24. Sykes RI. An asymptotic theory of incompressible turbulent boundary-layer flow over a small hump. *Journal of Fluid Mechanics* 1980; **101**: 647.
25. Kuzan JD, Hanratty TJ, Adrian RJ. Turbulent flows with incipient separation over solid waves. *Experiments in Fluids* 1989; **7**: 88.
26. Wood N, Mason P. The pressure force induced by neutral turbulent flow over hills. *Quarterly Journal of the Royal Meteorological Society* 1993; **119**: 1233.

